Characterization of Interconnects for Perovskite Solar Modules

William Mitts

A thesis

submitted in partial fulfillment of the

requirements for the degree of

Master of Science

University of Washington

2023

Committee:

J. Devin MacKenzie

Tanka Rana

Program Authorized to Offer Degree:

Materials Science & Engineering

University of Washington

Abstract

Characterization of Interconnects for Perovskite Solar Modules

William Mitts

Chair of the Supervisory Committee:

J. Devin MacKenzie

Department of Materials Science & Engineering

Electrical characterization of interconnects for solar modules allows for accurate resistive loss assessment. Specifically, for thin-film perovskite solar modules, it is crucial to assess the resistive losses such as contact resistance and contact resistivity where the top and bottom electrodes meet. To overcome the difficulties in commercializing perovskite thin-film devices, it is pivotal to improve upon device fabrication and characterization procedures. Using a four-point probe system, multiple aspects of electrical characterization can be carried out with simple test structures resembling solar modules. Previously, this probe system has been used to characterize sheet resistance of semiconductors and resistance of the metal contacts, but less often has been used in the field of thin-film photovoltaics. Critically, the P2 interconnection where the cells in a module are serially connected has the potential to be further optimized to lessen resistive losses. In this work, specially constructed test structures resembling perovskite thin-film solar modules with P2 interconnects are electrically characterized utilizing a four-probe system and a transition line method.

1. Introduction

Perovskites are a class of material composed of either an organic-inorganic hybrid or an all-inorganic structure which was discovered over one hundred years ago. Over the last few years, perovskite-based solar cells and modules have made a tremendous leap forward and are continuing to improve. Working based on the photoelectric effect, these devices harness the energy from the sunlight by absorbing this energy and exciting electrons to drive a current. Specifically, these devices are known as photovoltaic (PV) cells or modules. Compared to more traditional silicon-based solar cells, perovskites have seen a tremendous increase in efficiency. For example, single-junction cells have a current maximum efficiency of 26.1 % which was achieved over the course of nearly 40 years.[1] Starting at 14.1 % in 2014 and quickly progressing to 25.7 % as of 2022, perovskites are developing at an astounding rate when compared to silicon cells.[2] The efficiencies of many different solar cells are shown below in **figure 1**.

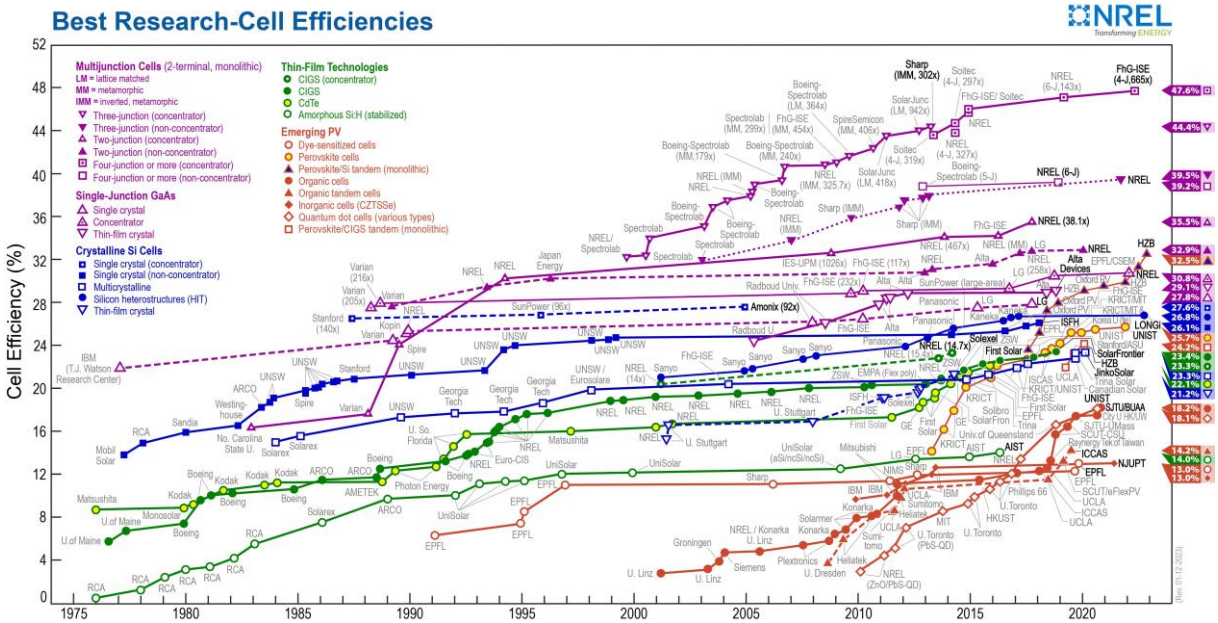

Figure 1**.** Chart of the best research cell confirmed conversion efficiencies for many types of photovoltaic cells. Perovskite solar cells are depicted with a yellow circle and an orange outline[1].

Perovskites are used as the absorber material perovskite-based solar cells. The first perovskite calcium titanium oxide was discovered by mineralogist Gustavus Rose in 1839. The general crystal structure of these materials takes the form of ABX_3 where 'A' is the positively charged cation as well as 'B' while the 'X' is the anion that bonds to both components. While a large number of components can be interchanged to create various perovskite materials, methylammonium lead halide is the most common. In this structure, the 'A' site is occupied by the methylammonium (MA), 'B' is occupied by the lead (Pb) and the 'X' site is typically iodine (I), bromine (Br), or chlorine (Cl). A generic perovskite structure is shown below in **figure 2**. Methylammonium lead Iodide ($CH_3NH_3PbI_3$) is one of the most common perovskites for solar cell absorber materials and is abbreviated as $MAPbI_3$.[3]

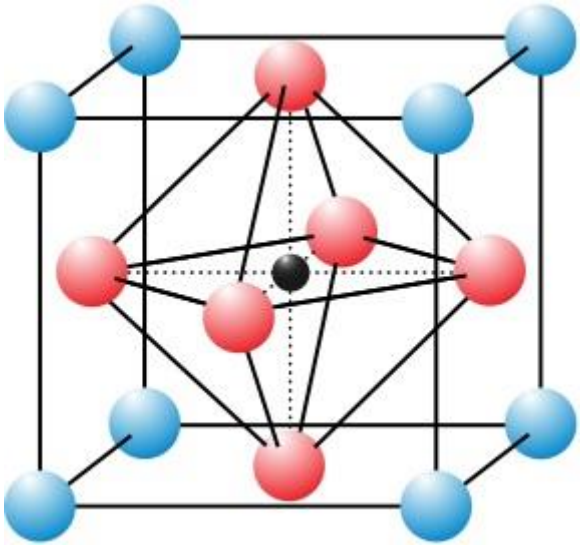

Figure 2**:** Crystal structure of a typical perovskite lattice. The blue spheres are the 'A' site, the black sphere is the 'B' site, and the red spheres are the 'X' site.[4]

One of the most appealing features of perovskite materials is their ability to interchange chemical components. For instance, very complex structures such as $Cs_{0.025}FA_{0.475}MA_{0.5}Sn_{0.5}Pb_{0.5}I_{2.925}Br_{0.075}$ are considered perovskite materials and can be tuned to provide desirable features not present in other simple structures.[5] However, substituting in many other elements such as cesium (Cs), formamidinium (FA), and others can lead to undesirable features such as an increase in toxicity, fragility, and water sensitivity. Another advantage perovskites have over more traditional materials in solar devices is their ability to

be solution processable. This allows the material to be easily deposited on a substrate and processed using roll-to-roll or sheet-to-sheet printing. As a result, perovskite materials could be easily scaled up for manufacturing and pose a reasonable solution for the impending energy crisis.[6] With this roll-to-roll technique, manufacturing cells could lead to a lower production cost and a much greater throughput with less energy involved.

The electronic properties of perovskites are relatively unique in that they can be tuned as previously mentioned by changing out chemical components in the crystal structure. As a result, these materials can have a wide variety of different bandgaps (BG) which are crucial to harnessing the power of sunlight. As shown by the work of Osbel Almora and coworkers, perovskites can have a bandgap ranging from 1.12 eV to 2.48 eV.[2] The Shockley-Queisser limit details the maximum theoretical efficiency of a solar cell that uses a single p-n junction to collect power at AM1.5. According to this theorem, the ideal semiconductor would have a bandgap of approximately 1.4 eV to extract the most power.[7] Thus, it is pertinent that materials with desirable bandgaps be used when making PV devices so the most amount of power is extracted. Besides bandgap tunability, when compared to other absorber materials for solar cells, perovskites have been shown to possess a lower loss in potential, large carrier mobility, and a large diffusion length.[8] The lower loss in potential means the cells could be tuned to have a much greater efficiency than other emerging solar technologies as seen by their rapid growth in **figure 1**. To further contribute to efficiency growth, the longer diffusion length in perovskites allows for a decrease in the exciton recombination as the charges have the opportunity to move further in the materials before recombining. This is further enhanced by the carrier mobility as this allows the charge carriers to move easily throughout the material.

A typical perovskite solar cell contains a stack from top to bottom consisting of glass, ITO, ETL, perovskite, HTL, and some metal contact such as gold or silver as shown in **figure 3a**. As the lab scale efficiency of PSCs continues to soar, the next step is to develop large-area

devices that have a high PCE, low cost, and great stability. With a PCE of 16.7% for a roll-to-roll fabricated PSC, Sutherland, and coworkers are improving these areas of PSC production.[9] What's more, they opted to fabricate the cells in ambient conditions and utilized printed electrodes based on electrically conductive pastes as opposed to a more commonly used process of thermal evaporation. Simply put, the solar module consists of monolithic serially interconnected solar cells. While this is a simple definition, producing modules has proven more difficult than single cells. When upscaling cells to module architecture, other factors are introduced that decrease the overall efficiency of the device. Most notably, the interconnection of cells in a module has been shown to contribute greatly to the overall module losses.[10–12] When the cells are interconnected, this creates a variation in the output voltage of the module. As a result of the interconnected geometry, inactive zones are produced leading to a decrease in the geometric fill factor (GFF). The GFF is defined as the ratio of the active area to the aperture area of the solar module with the highest GFF achieved being 99%.[13] To connect these solar cells in the modules, three interconnections are created; P1, P2, and P3. The P1 interconnection disconnects the bottom electrode and defines the cell dimension. P2 patterning removes all layers above the bottom electrode and connects the top electrode to the bottom electrode to interconnect neighboring cells. Finally, P3 patterning disconnects the top electrode.[14]

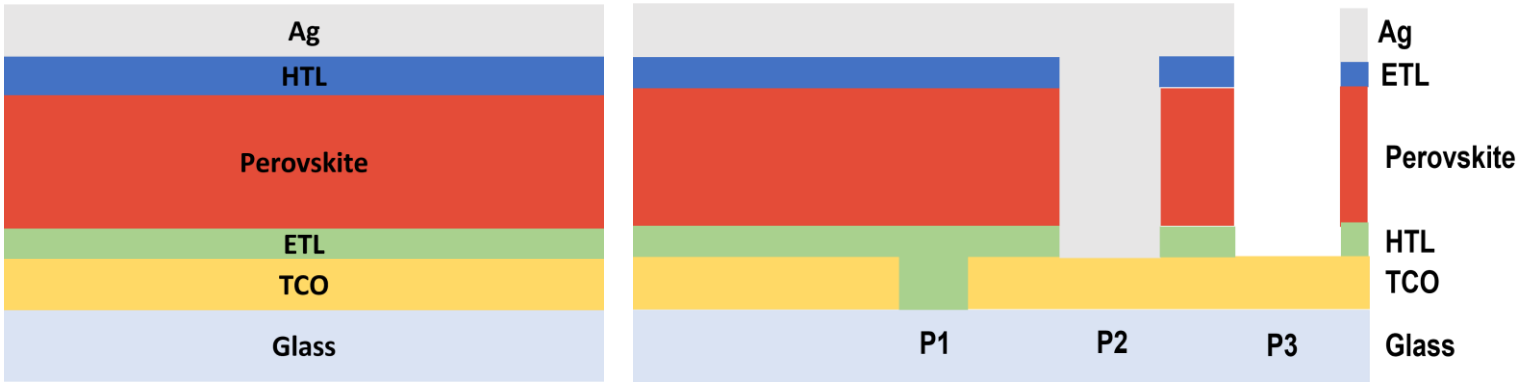

Figure 3: (a) Typical perovskite solar cell stack. (b) Cross section of a planar perovskite module with P1, P2, and P3 scribes.

It is normal to either laser pattern or mechanically scribe the lines to achieve interconnects in solar modules. Since interconnections are used to electrically connect the solar cells within the module, there must be a resistance value associated with this connection. This assumption leads to the contact resistance between the top and bottom electrode which contributes to the resistance of the interconnection. As such, it is pertinent to optimize cell design for highly efficient modules by analyzing contact resistance. Here, we compare laser patterned P2 scribes of 1.0, 1.5, and 2.0 mm long through characterization methods utilizing a custom 4-point probe, transition line method, and optical profilometry.

2. Methods

2.1 *Silver/ITO Test Structures: Sample Processing*

The first set of test structures was created to measure the contact resistance between indium tin oxide (ITO) and silver by utilizing the transition line measurement (TLM). This was done to ensure the 4-point probe station and our methods were consistent with previously determined literature values of contact resistance for silver/ITO structures. The samples were created using Delta Technologies, Limited ITO on unpolished float glass substrates with a sheet resistance (R_{Sh}) of 12 – 20 Ω. The three structures had dimensions of 100 x 100 x 1.1 mm. ITO/glass samples were washed using detergent, deionized (DI) water, and isopropanol and dried using a nitrogen gun to ensure no undesirable particulates were on the surface.

2.1.2 *Silver/ITO Test Structures: Mask and Silver Contacts*

The first mask used on sample 1 was created by an unconventional method utilizing Kapton tape. This was a quick and easy method to make a mask in an hour as opposed to having a metal mask made which takes much longer. Kapton tape was cut using a razor blade into the desired distance between silver contacts of 16mm, 2mm, 4mm, 8mm, 16mm, 32mm, and 16mm as depicted below in **figure 4**. Using the same feature sizes as the Kapton tape

mask, a mask made of polylactic acid (PLA) was 3D printed using the Ultimaker 3D printer at the Washington Clean Energy Testbeds. This was done to create a mask that could be reused as opposed to a Kapton tape mask that would need to be recreated for every test structure. The printed mask was used to fabricate the other two silver/ITO test structures. Once the masks were finished printing, any undesired pieces or features of PLA were cut off using a razor. Once the cleaning was finished, the masks were placed in a nitrogen glovebox to degas.

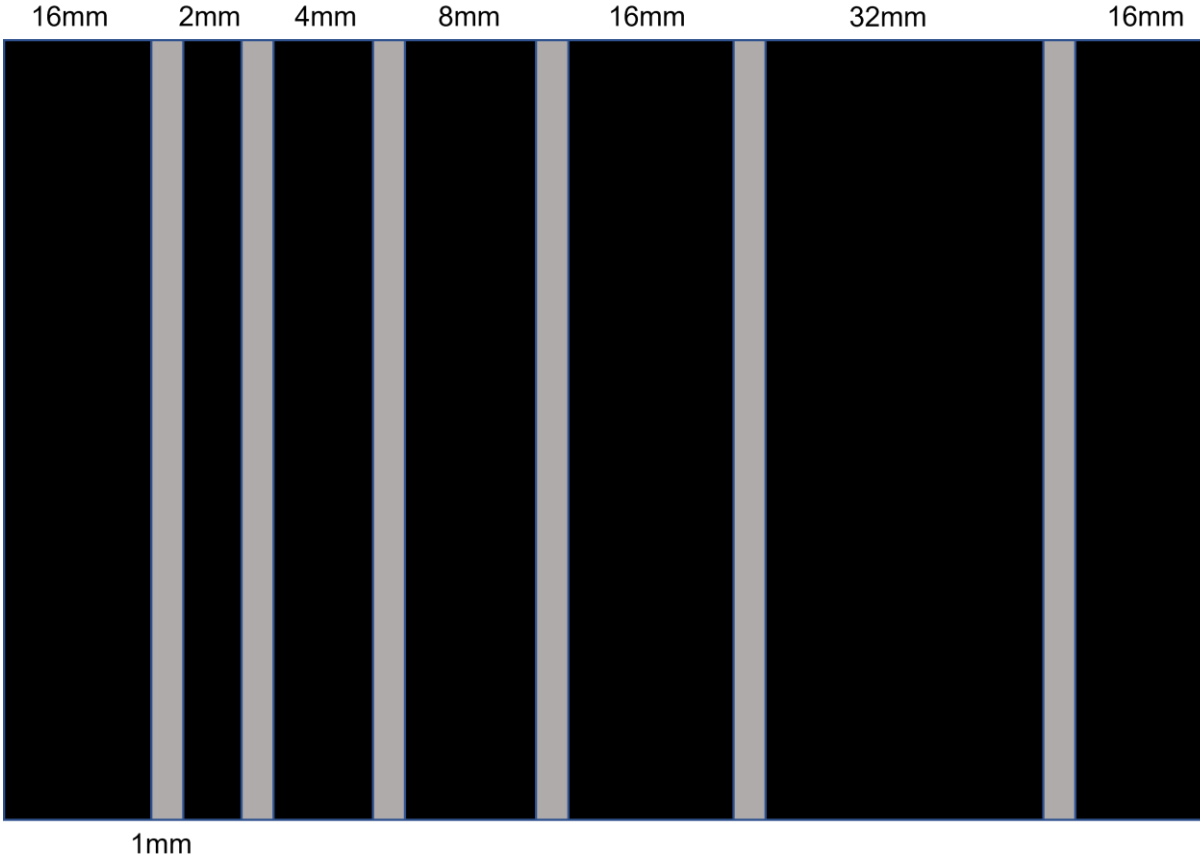

Figure 4: Silver/ITO mask design for test samples. The black indicates the portion covered by the Kapton/plastic whereas the silver lines represent the area silver is deposited. Each silver line is 1 mm long and 100 mm wide.

Deposition of the silver contacts for the test structures was done using the thermal evaporator in the Research Training Testbed at the University of Washington. The thermal evaporator was housed in a nitrogen glovebox and each sample was individually evaporated on as only one 100 x 100mm sample can fit in the evaporator at a time. 99.99% Silver pellets were placed in the boat and the evaporator chamber was pumped down for at least 15 minutes

to a pressure below $1x10^{-6}$ torr. Silver was deposited at a rate of 1 Å/s. The first test structure had 126 nm of silver evaporated onto the sample while the second and third test structures had 200 nm. Once evaporations were finished, the samples were removed, and the evaporator was vented and pumped back down to a pressure below $1x10^{-6}$ torr to ensure cleanliness. The finished test structure is shown in **figure 5**.

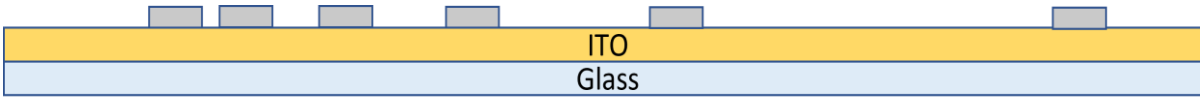

Figure 5: Silver/ITO/Glass test structure. The light blue depicts glass, yellow represents ITO, and the gray represents the silver contacts for all three test structures.

2.1.3 *Silver/ITO Test Structures: Profilometry and Transition Line Measurements*

The line widths of silver deposited onto the ITO/glass substrates were verified through optical profilometry via a laser scanning digital microscope as this would not risk damaging the thin silver contacts. Specifically, an Olympus LEXT OLS4100 at the Washington Clean Energy Testbeds was used with 1x magnification to identify the line widths. The average width of the contacts in each device was then used for data processing.

To conduct electrical measurements for the transition line method test structures, a custom four-point probe setup was connected to a Keithley 2450 Source-Measure unit. The probe station consisted of four FormFactor DC positioners, four probe arms, and four 1.5 μm probe tips connected to the Keithley 2450 Source-Measure unit via a triax/BNC cable for maximum shielding. The probe stands were magnetically secured to the base of the station for greater stability. Samples were placed at the center of the probe station on an XY adjustable metal plate. To ensure the probes were placed accurately on the test structures during measurements, a camera fitted to an adjustable rod was placed above the probe station and connected to a computer monitor. Within the Keithley KickStart software, parameters such as voltage, current, measurement limit, and number of measurements can be adjusted. The transition line measurement gauges the voltage drop between two contacts in the silver/ITO

test structures, so a current bias of 1 μA was applied instead of a voltage sweep. The 4-wire terminal was also needed in order to utilize the individual sense high, sense low, source high, and source low probes. 3M conductive copper foil tape was used to check that all electrical connections and probes were working properly given its known resistance value of $0.010\ \Omega/in^2$. Fifty-one sets of measurements were taken for each of the pairs of contacts on the test structures and the resistance values were averaged for further calculations and data processing using Microsoft Excel.

2.2 *P2 Contact Resistance Devices: Sample Processing*

All materials used for the P2 devices were used as received without further purification. Methylammonium iodide (MAI, > 99.99%, Greatcell), formamidinium iodide (FAI, > 99.99%, Greatcell), cesium iodide (CsI, 99.999%, metal basis, Sigma Aldrich), lead iodide (PbI2, 99.999%, TCI), lead chloride (PbCl2, >99.0%, TCI), methylammonium chloride (MACl, >99.5%, Greatcell), poly[bis(4-phenyl)(2,4,6-trimethylphenyl)amine (PTAA) (Ossilla), 2-methoxyethanol (2ME, anhydrous, Sigma Aldrich), Acetonitrile (ACN, anhydrous, Sigma Aldrich), dimethyl sulfoxide (DMSO, anhydrous, Sigma Aldrich), isopropanol (IPA, Sigma Aldrich), C60 (98%, Sigma Aldrich), bathocuproine (BCP, 96%, Sigma Aldrich)

Like the silver/ITO test structures, the P2 devices were created using Delta Technologies, Limited ITO on unpolished float glass substrates with a sheet resistance (R_{Sh}) of 12 – 20 Ω. These devices were created to measure the contact resistance of our full stack perovskite solar cell recipe for future module production and determine if contact resistance contributes to our single-cell design. Different solar cell designs have different interfaces in which the contact resistance can vary due to different materials and feature sizes. Therefore, we found it important to characterize our cell recipe with similar feature sizes. Starting with an ITO/glass sheet with dimensions of 100 x 100 x 1.1 mm, ITO/glass samples were washed using detergent, deionized (DI) water, isopropanol, and dried using a nitrogen gun. Once

cleaned, the ITO/glass sheet was then cut into 3 pieces 33.33 mm wide and 100 mm long to create three different devices with P2 scribes of 1.0, 1.5, and 2.0 mm. These sizes were chosen to best reflect the gap in the single-cell devices electrode design of 1.5 mm. Samples were cut using a nanosecond UV laser (352 nm) controlled by EZcad software. Processing occurred in a controlled environment room (CER) with relative humidity no greater than 30%. The samples were stored in a large petri dish in the CER until further processing and layer deposition.

2.2.2 *P2 Contact Resistance Devices: Mask Design*

The mask design for the P2 contact resistance devices was optimized to obtain the most amount of data per thermal evaporation as this step takes the most time. Instead of creating one mask for each device, two masks were made to fit three samples at a time. The masks were printed using the Ultimaker 3D printer at the Washington Clean Energy Testbeds with PLA as previously mentioned. One mask was designed to deposit the ETL layers while the other was used to deposit the silver contacts on the P2 scribes. The ETL mask is needed to block the P2 scribes during thermal evaporation to prevent ETL from filling the trenches. If not successfully done, no current path could be established between silver contacts to accurately represent the scribes in a solar module. The ETL mask consists of 3 sections for the three devices: the bottom 1/3 fits the 1mm long trench device, the middle section fits the 1.5 mm devices, and the top portion fits the 2.0 mm long trench device. Furthermore, the silver contact mask is needed to prevent the deposition of silver over the entire surface of the device and direct it to fill the P2 trenches, so the top and bottom electrodes are connected. Analogous to the ETL mask, the silver contact mask fits the same devices in the same place. However, the silver mask exposes the P2 trenches and extends 0.5 mm on both sides of each scribe line. This was done to ensure silver was evaporated on top of the ETL layer and filled the P2 trench. Both masks have an additional 0.75 mm of space on all sides to properly fit the devices inside. In other words, the devices are centered inside a 101.5 mm square. The

specific geometries of both the ETL and silver mask are shown below in **figure 6a** and **6b,** respectively.

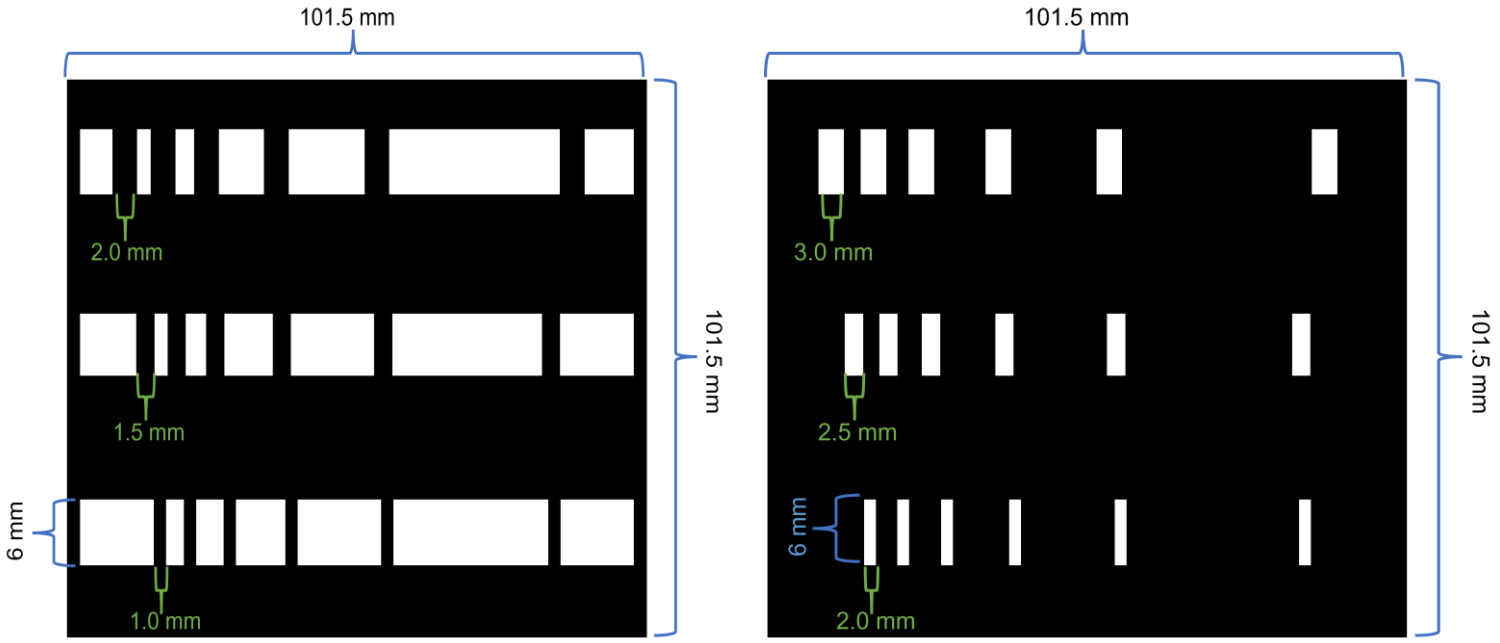

Figure 6: a) Mask geometry of the ETL mask for P2 contact resistance devices printed using PLA. Spacing between the mask lines are 2, 4, 8, 16, and 32 mm for all three sections. b) Mask geometry of the silver contact mask P2 contact resistance devices printed using PLA.

2.2.3 *P2 Contact Resistance Devices: Device Stack and Electrical Measurements*

The P2 contact resistance devices were created to mimic the interconnects for a perovskite minimodule using the recipe from our lab. The recipe consists of glass/ITO/PTAA/perovskite/C60/BCP/Ag. The following list depicts each materials role in the solar cell; glass is the substrate, ITO is the front contact, PTAA is the hole transport layer (HTL), perovskite is the photo absorber, C60 is the electron transport layer (ETL), BCP allows for greater electron extraction and better blocking of excitons, and finally silver is the back contact.

As previously mentioned, one slide of ITO/glass was cut into three sections using the nanosecond UV laser. Once cut, the slides were cleaned slightly differently from the previous devices. ITO substrates were cleaned by sonication in DI water with 2% detergent, acetone, and ethanol. Substrates were then treated with UV-Ozone for 10 minutes. The hole transport

layer PTAA (3 mg/ml) was deposited onto the cleaned ITO substrate by slot-die coating. The coating conditions for the PTAA were an ink flow rate of 100 μl/min at a coating speed of 70 cm/min. The distance between the slot-die head and the substrate was ~34 μm with a substrate temperature of 40 °C. After coating, the PTAA was annealed at 100 °C for 10 minutes. A precursor solution consisting of 1.15M $FA_{0.25}MA_{0.75}PbI_3$ was prepared by dissolving it in acetonitrile and 2-methoxyethanon (3:1). To that solution, CsI (2%), MACl (5%), DMSO (15%) to create the perovskite solution. The perovskite layer was then deposited on PTAA/ITO/Glass by slot die coating. The coating conditions for the perovskite deposition were an ink flow rate of 150 μl/min with a coating speed of 100 cm/min. The slot die head was ~60 μm away from the substrate during coating at room temperature in the CER. The perovskite film was then annealed at 100 °C for 10 minutes.

Using the UV laser, each respective slide of Perovskite/PTAA/ITO/Glass was placed onto the metal plate and patterned to remove excess ITO. A raster scan ablation along with a full lasing of the perimeter of the desired shape was used to ensure all edges of the designs were as defect-free as possible. After removing excess ITO, a rectangle with dimensions of 80 x 6 mm was patterned on the substrate to remove Perovskite/PTAA/ITO where not necessary. The 80 x 6 mm slide dimensions were then used for the P2 scribe devices. To create the P2 scribes for each device, laser parameters were changed when strictly removing the Perovskite/PTAA layer to not damage the ITO underneath. Using the laser conditions for the previous pattern would ablate the ITO layer and not create a P2 contact. A set of 6 P2 scribes of 1.0, 1.5, and 2.0 mm were created, one set of sizes for each device. After patterning, the three devices were vacuum sealed and transported to the RTT for thermal evaporation of the C60, BCP, and silver. The evaporation conditions are the same as for the silver/ITO devices mentioned previously. Using the ETL mask, 30 nm of C60 were deposited on the perovskite layer at a rate of 0.2 Å/s for the first 5 nm and then increased to 0.5 Å/s for the remaining

25 nm. Next, 7 nm of BCP was deposited on top of C60 at a rate of 0.2 Å/s. Finally, the mask was then switched to the silver contact mask, and 200 nm of silver was evaporated at a rate of 0.5 Å/s for 10 minutes to ensure even deposition. The rate is then increased to 1 Å/s for the remaining 190 nm. The devices were then stored in a nitrogen glovebox out of the light until measurements were conducted.

Electrical measurements were carried out the same way as previously mentioned using a custom four-point probe setup connected to a Keithley 2450 Source-Measure unit. The four probes were placed in the following layout: the source high probe was placed on the left contact while the source low probe was placed on the right contact. In front of the source high probe, the sense high probe was placed as close as possible. Finally, the sense low probe was placed on the right contact directly across from the sense low probe. **Figure 7** depicts the probe placement for conducting the transition line measurements on the P2 devices.

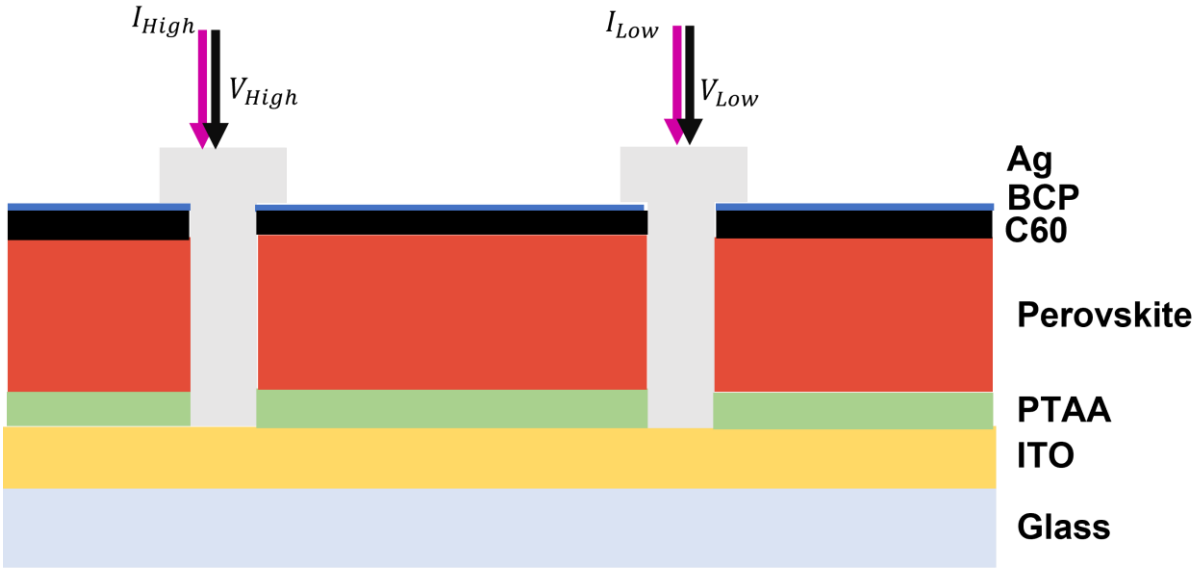

Figure 7: Transition line measurement of the P2 scribe devices with probe placement. The force-high (I_{High}) and low probes (I_{Low})are shown as pink arrows while the sense-high (V_{High}) and low (V_{Low}) probes are shown as black arrows. Current will flow from the force-high probe through the left silver contact down into the ITO and up through the force-low probe. The voltage drop between these two points is measured by the sense-high and sense-low probes.

3. Results and Discussion

3.1 *Characterization of Silver/ITO Test Structures and P2 Devices*

To ensure that our methods were consistent with previously determined literature values of contact resistance for silver/ITO structures, the Silver/ITO test structures were created with 1 mm long silver contacts at a width of 100 mm. Optical profilometry via a laser scanning digital microscope was used to ensure the silver patterning on each test structure was 1 mm long. Each contact must be as close to 1 mm as possible as this can negatively impact the contact resistance calculations. It was determined that for test structure 1 (TS1) made with Kapton tape, the contact length was an average of 1.09 mm resulting in a length deviation of about 9%. Test structure 2 (TS2) on the other hand was unable to be tested as the contacts did not connect the entire width of the ITO/glass substrate. This error is most likely due to an error in cleaning the mask with the razor blade where some of the PLA was not sufficiently smoothed out or removed. The third test structure (TS3) accounted for this error and all silver contacts traveled the full width of the ITO/glass sheet. The average contact length for TS3 was 1.44 mm resulting in a length deviation of about 44%. A significant increase in the relative contact length error was most likely due to mask warping during thermal evaporation due to increased temperature in the evaporator. The printed mask had accurately displayed 1 mm sized lines, so printing inaccuracies were not determined as the issue. Given more time, a metal mask would be desirable as they do not warp under evaporation conditions.

For the P2 contact resistance devices, P2 scribes were within 10 μm of the desired 1.0, 1.5, and 2.0 mm line lengths as that is the tolerance for the nanosecond UV laser used for patterning. Complete removal of the PTAA/Perovskite is assumed as previous users have confirmed complete removal with the settings used here for scribing.

3.2 *Electrical Measurements: Transition Line Method*

Electrical characterization of both devices utilizes the transition line method via a four-probe setup to measure the resistance between the top and bottom electrodes.[14–16] As mentioned in sections 2.1.3 and 2.2.3, the specific probe geometry was used to characterize both devices. The contact resistance (R_C) with units of ohms (Ω) was determined for both test structures and P2 devices. Notably, the contact resistance is an area-dependent quantity that is influenced by the metal/semiconductor interface. As a result, the specific contact resistivity (ρ_C) is used in its place. Contact resistivity is an area independent quantity with units of $\Omega - cm^2$.

In the case of contact resistance measurements, the current travels laterally from one electrode to another as the metal electrodes and semiconductor are in a planar geometry. The contact resistance is then measured between variably spaced contacts as in figure 7. In **figure 8** below, a more generalized version is shown for clarification.

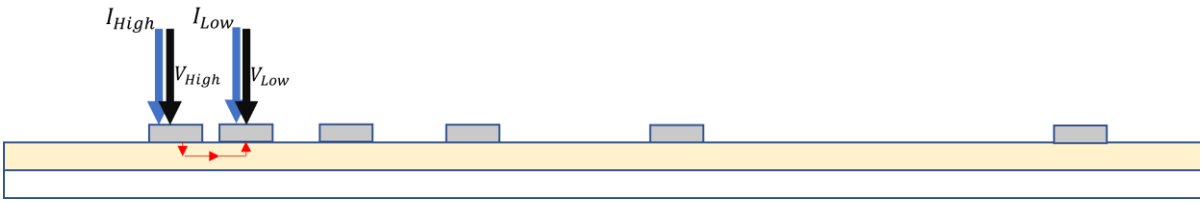

Figure 8: Variably spaced contacts for the transition line method. The grey bars represent the contacts, the yellow represents the semiconductor, and the red arrows represent the current flow between contacts.

While using a special test structure as opposed to a solar cell is not ideal, the busbar connections of solar cells can introduce issues such as shorting and potential series resistance.[16] For the silver/ITO structures, the width (W) of the contacts were 100 mm, while the length of the contacts were 1 mm. The spacing between contacts (d) from left to right for both devices were 2, 4, 8, 16, and 32 mm. Instead of directly using the contact geometry, the transfer length (L_T) is used as the current flow into the contacts may not be uniform and is taken to be the effective length of the contact. This is because the current that flows in or out

of the contacts can vary greatly at the edges and is known as current crowding. The equation for transfer length is as follows:

$$L_T = \sqrt{\left(\frac{\rho_C}{R_S}\right)} \tag{1}$$

Where R_s is the sheet resistance of the semiconductor layer. From here, the contact resistance can be written as:

$$R_C = \frac{\rho_C}{L_T \cdot W} = \frac{R_S \cdot L_T}{W} \tag{2}$$

Fundamentally, the quantity $L_T \cdot W$ can be thought of as the effective area of the contacts. With this information, the total resistance R_T can then be described as the sum of the resistance of the semiconductor layer and the current entering and exiting the contacts. Since the current is both entering and exiting the contacts, R_C is multiplied by a factor of 2. The equation for the measured total resistance is as follows:

$$R_T = \frac{R_S \cdot L}{W} + 2\frac{\rho_C}{L_T \cdot W} = \frac{R_S \cdot L}{W} + 2\frac{R_S \cdot L_T}{W}$$

$$R_T = \frac{R_S}{W}(L + 2L_T) \tag{3}$$

Putting it all together, creating a plot of R_T vs L will yield $2R_C$ as the y-intercept by extrapolation back where $L_T = 0$. Furthermore, extrapolation to the x-intercept leads to $-2L_T$ and thus we can utilize the transition line method for contact resistivity calculations. Example calculations for R_C, R_S, L_T, and ρ_C are shown below for TS1 taking data from **figure 9** depicting the TLM graph for TS1.

$$R_C = \frac{3.295}{2} = 1.647\ \Omega$$

$$R_S = slope \times W = 2.518\,\frac{\Omega}{cm} \cdot 10\ cm = 25.18\ \Omega/\square$$

$$L_T = \frac{3.295}{2 \cdot 2.518} = 0.654\ cm$$

$$\rho_C = R_C \cdot L_T \cdot W = 1.647\ \Omega \cdot 0.654\ cm \cdot 10\ cm = 10.8\ \Omega\text{cm}^2$$

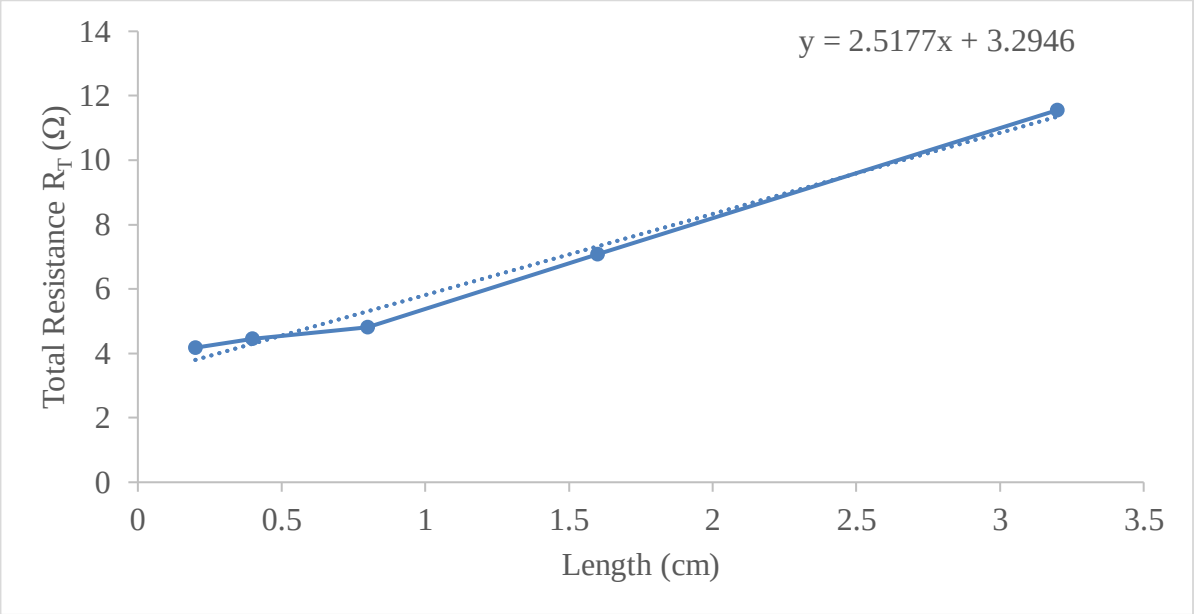

Figure 9: Plot of total resistance vs distance between contacts for TS1. The dotted blue line is fit to determine the slope and y-intercept for further calculations.

Table 1: Data calculated from the TLM measurements for Silver/ITO test structures and P2 devices.

Device	R_C (Ω)	R_S (Ω/□)	L_T (cm)	ρ_C (Ωcm^2)
TS1	1.65	25.18	0.65	10.8
TS3	1.99	16.24	1.23	24.4
P2 (1 mm)	6.75	99.48	0.23	0.92
P2 (1.5 mm)	11.32	96.22	0.39	2.66
P2 (2 mm)	8.38	88.22	0.32	1.59

Data for both TS1, TS3, and P2 contact resistance devices are in **Table 1**. TS1 had a relatively high sheet resistance of 25.18 Ω/□ compared to the listed sheet resistance of the ITO between 12 – 20 Ω while TS3 falls within the range. This is more than likely due to the greater slope value when compared with that of TS3. However, TS3 was shown to have a much greater variation in the contact line lengths mentioned in section 3.1. As a result, this is most likely the cause of the much larger L_T and ρ_C values of 1.23 cm and 24.4 Ωcm^2, respectively. That being said, neither test structure exhibited contact resistivity in line with

literature values for 10 Ω/□ ITO of 3.55 X 10^{-2} Ωcm^2.[17] One major factor could be the leading cause for this error; either some or all of the probe tips are puncturing the silver film. It was confirmed through optical profilometry that probe tips had punctured the surface when examining contact lengths. However, we are not sure if this occurred for every probe tip at each measurement.

Figure 10 shows puncture holes highlighted with red circles from the tip making too forceful contact with the silver. In the future, a better system for identifying contact height will need to be established by using another observation method such as a second camera parallel to the measurement plate. Alternatively, silver paste could be placed on the contacts where the measurements would be taken to increase the thickness of the silver to reduce the likeliness of puncture. In the early stages of testing, various probe tips made from copper wire, other probe arms, and micro positioners were tested to prevent this issue, but all ended with an inconsistent electrical reading due to electronic issues with the connections.

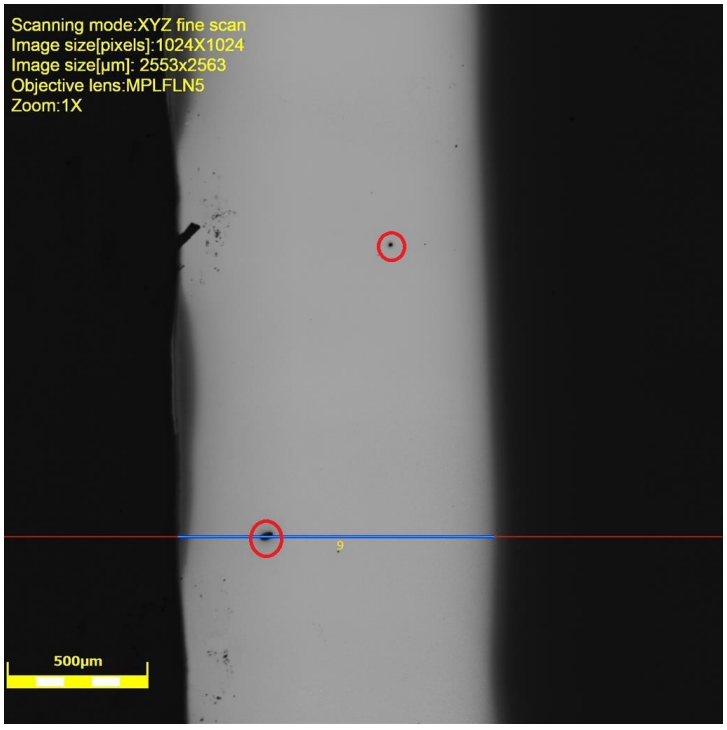

Figure 10: Puncture holes in silver film are outlined with red circles and are believed to be from probe tips during TLM testing.

For the P2 contact devices, the same set of measurements was carried out along with the same distances between each of the contacts. It is important to note that the length of the P2 scribe is being used for calculations, not the length of the silver at the top of the stack. This is because the current is confined to the P2 contact and not traveling elsewhere atop the structure. Furthermore, this work does not account for the sheet resistance of the silver which has been shown to contribute to contact resistance value, albeit very minimal for gold having resistance values of 0.09 Ω for laser patterned contacts.[14] Calculated values for the same parameters are shown in table 1 while the graph for the fitted lines of all P2 devices is shown in **figure 11** below.

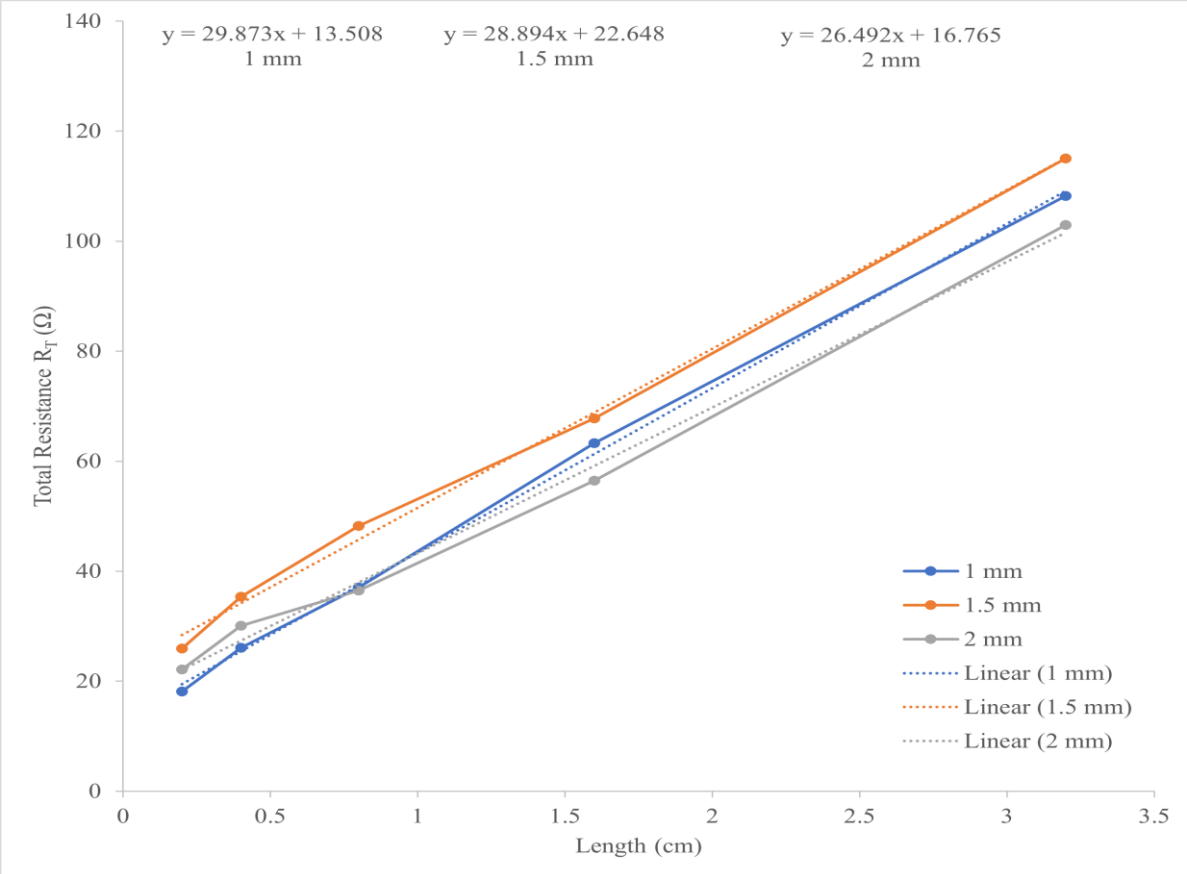

Figure 11: Plot of total resistance vs distance between contacts for P2 devices. The dotted lines are fit to determine slope and y-intercept for further calculations for each respective device.

Both the 1 mm and 1.5 mm P2 devices were shown to have great linearity while the 2 mm device deviated slightly. Why this may specifically be is unclear at the moment, but any

of the previously mentioned issues such as film puncture could have been a cause. Conversely, the transfer length and contact resistivity for all P2 devices were significantly closer to literature values, most likely due to user experience. Most notably, the 1.0 mm P2 device with a contact resistivity of 0.92 Ωcm^2. Manually manipulating each probe to takes a good sense of dexterity and experience. The test structures were developed early on when minimal testing had occurred. Therefore, the more desirable values can partially be attributed to a greater sense of probe positioning and dexterity. It was expected that the contact resistance of each device would increase as the P2 scribe length increased. That is not clear with this work since the 1.5 mm scribe size device yielded a much greater relative contact resistance when compared to the 2 mm scribe size. The best guess as to why this occurred is due to the mask warping issue previously mentioned, except this time the C60 or BCP could have evaporated in the P2 trench not allowing the silver to make complete contact with the ITO. Conversely, the specific contact resistivity for all three P2 devices was relatively close to one another, showing they are consistent if nothing else. Once again, these values are still larger than what the literature has reported for gold contacts with a value of $\rho_C = 3\ X\ 10^{-4}$ Ωcm^2 as no literature could be found on silver contacts.[14] This either means there is a consistent unidentified issue during the measurement process, or that our cell recipe and design need further optimization.

Conclusion and Future Work

With perovskite materials making a tremendous leap forward in the last 40 years as the photoactive layer in solar cells, greater optimization of individual module geometry is increasingly important for further development in minimizing resistive losses. Electrical characterization through four-point probe methods has delivered promising results for interconnection optimization in tandem with device modeling. Accurate electrical characterization of modules and cell recipes greatly minimizes resistive losses by identifying potential issues within the devices such as contact and sheet resistance which contribute to the

overall power conversion efficiency. In turn, this propels the development of highly efficient thin-film solar modules and leads to potential cost reduction in manufacturing costs.

In future work, the primary focus would be on optimizing the measurement method with the four-point probe. According to other literature reports, our contact resistivity was shown to be significantly greater by four orders of magnitude. While other issues such as PLA mask warping could have led to some of these issues, it is most likely that the probe tips were puncturing the silver film at some point in the measurement process, leading to greater resistance readings as they could have contacts the ETL or ITO layer. This could be mitigated through a better probe monitoring step via additional video cameras or by using probe tips with a flat surface. Additionally, creating devices through alternative patterning methods to compare electrical features would also be useful. Other literature has reported contact resistivity of mechanically scribed interconnects, but none have reported chemically scribed interconnects via super inkjet printing using chemical solutions. Further study into this form of patterning could be a potential pathway to more energy-conscious and waste-free patterning techniques.

Acknowledgments

Through the collective efforts of Professor J. Devin MacKenzie, Phillip Cox, Tanka Rana, Ethan Schwartz, Mazhar Abbas, and all the collaborators within the Photovoltaics group, I greatly appreciate the support and guidance you have given me to allow me to conduct this work.

References

(1) *Best Research-Cell Efficiency Chart*. https://www.nrel.gov/pv/cell-efficiency.html (accessed 2023-03-12).
(2) Almora, O.; Baran, D.; Bazan, G. C.; Cabrera, C. I.; Erten-Ela, S.; Forberich, K.; Guo, F.; Hauch, J.; Ho-Baillie, A. W. Y.; Jacobsson, T. J.; Janssen, R. A. J.; Kirchartz, T.; Kopidakis, N.; Loi, M. A.; Lunt, R. R.; Mathew, X.; McGehee, M. D.; Min, J.; Mitzi, D. B.; Nazeeruddin, M. K.; Nelson, J.; Nogueira, A. F.; Paetzold, U. W.; Rand, B. P.; Rau, U.; Snaith, H. J.; Unger, E.; Vaillant-Roca, L.; Yang, C.; Yip, H.-L.; Brabec, C. J. Device Performance of Emerging Photovoltaic Materials (Version 3). *Adv. Energy Mater.* **2023**, *13* (1), 2203313. https://doi.org/10.1002/aenm.202203313.
(3) Mamaeva, M. P.; Samsonova, A. Yu.; Murzin, A. O.; Lozhkina, O. A.; Murashkina, A. A.; Selivanov, N. I.; Kapitonov, Y. V. Ultrafast Random Lasing in MAPbI3 Halide

Perovskite Single Crystals. *J. Phys. Chem. C* **2022**, *126* (46), 19816–19821. https://doi.org/10.1021/acs.jpcc.2c06114.
(4) Korjus. *Eesti: Perovskite*; 2011. https://commons.wikimedia.org/wiki/File:Perovskite_ABO3.jpg (accessed 2023-05-08).
(5) Kapil, G.; Bessho, T.; Sanehira, Y.; Sahamir, S. R.; Chen, M.; Baranwal, A. K.; Liu, D.; Sono, Y.; Hirotani, D.; Nomura, D.; Nishimura, K.; Kamarudin, M. A.; Shen, Q.; Segawa, H.; Hayase, S. Tin–Lead Perovskite Solar Cells Fabricated on Hole Selective Monolayers. *ACS Energy Lett.* **2022**, *7* (3), 966–974. https://doi.org/10.1021/acsenergylett.1c02718.
(6) *Roll-to-Roll Printing of Perovskite Solar Cells | ACS Energy Letters*. https://pubs.acs.org/doi/10.1021/acsenergylett.8b01556 (accessed 2023-02-19).
(7) Ehrler, B.; Alarcón-Lladó, E.; Tabernig, S. W.; Veeken, T.; Garnett, E. C.; Polman, A. Photovoltaics Reaching for the Shockley–Queisser Limit. *ACS Energy Lett.* **2020**, *5* (9), 3029–3033. https://doi.org/10.1021/acsenergylett.0c01790.
(8) *The expanding world of hybrid perovskites: materials properties and emerging applications - PMC*. https://www.ncbi.nlm.nih.gov/pmc/articles/PMC4563667/ (accessed 2023-02-19).
(9) Li, H.; Zuo, C.; Angmo, D.; Weerasinghe, H.; Gao, M.; Yang, J. Fully Roll-to-Roll Processed Efficient Perovskite Solar Cells via Precise Control on the Morphology of PbI2:CsI Layer. *Nano-Micro Lett.* **2022**, *14* (1), 79. https://doi.org/10.1007/s40820-022-00815-7.
(10) Razza, S.; Di Giacomo, F.; Matteocci, F.; Cinà, L.; Palma, A. L.; Casaluci, S.; Cameron, P.; D'Epifanio, A.; Licoccia, S.; Reale, A.; Brown, T. M.; Di Carlo, A. Perovskite Solar Cells and Large Area Modules (100 Cm2) Based on an Air Flow-Assisted PbI2 Blade Coating Deposition Process. *J. Power Sources* **2015**, *277*, 286–291. https://doi.org/10.1016/j.jpowsour.2014.12.008.
(11) Yoon, J.-H.; Park, J.-K.; Kim, W. M.; Lee, J.; Pak, H.; Jeong, J. Characterization of Efficiency-Limiting Resistance Losses in Monolithically Integrated Cu(In,Ga)Se2 Solar Modules. *Sci. Rep.* **2015**, *5* (1), 7690. https://doi.org/10.1038/srep07690.
(12) Urban, T.; Heimann, M.; Schmid, A.; Mette, A.; Heitmann, J. Analysis of Ohmic Losses Due to Solder and Pressure Interconnection and Related Interface Resistances for Solar Cells. *Energy Procedia* **2015**, *77*, 420–427. https://doi.org/10.1016/j.egypro.2015.07.059.
(13) Rakocevic, L.; Schöpe, G.; Turan, B.; Genoe, J.; Aernouts, T.; Haas, S.; Gehlhaar, R.; Poortmans, J. Perovskite Modules with 99% Geometrical Fill Factor Using Point Contact Interconnections Design. *Prog. Photovolt. Res. Appl.* **2020**, *28* (11), 1120–1127. https://doi.org/10.1002/pip.3312.
(14) Rakocevic, L.; Gehlhaar, R.; Merckx, T.; Qiu, W.; Paetzold, U. W.; Fledderus, H.; Poortmans, J. Interconnection Optimization for Highly Efficient Perovskite Modules. *IEEE J. Photovolt.* **2017**, *7* (1), 404–408. https://doi.org/10.1109/JPHOTOV.2016.2626144.
(15) Frontmatter. In *Semiconductor Material and Device Characterization*; John Wiley & Sons, Inc.: Hoboken, NJ, USA, 2005; pp i–xv. https://doi.org/10.1002/0471749095.fmatter.
(16) Janoch, R.; Gabor, A.; Anselmo, A.; Dubé, C. Contact Resistance Measurement – Observations on Technique and Test Parameters; 2015. https://doi.org/10.1109/PVSC.2015.7355851.
(17) Rastogi, A. C.; Lakshmikumar, S. T. Indium-Tin-Oxide-Metal Interfacial Resistance and Its Implication for Solar Cells. *Sol. Cells* **1989**, *26* (4), 323–328. https://doi.org/10.1016/0379-6787(89)90091-4.